ACADEMIC PRESS

Available online at www.sciencedirect.com

SCIENCE DIRECT®

Journal of Sound and Vibration 261 (2003) 225–245

JOURNAL OF SOUND AND VIBRATION

www.elsevier.com/locate/jsvi

# Analysis of the flow-induced vibrations of viscoelastically supported rectangular plates

Junhong Park, Thomas Siegmund, Luc Mongeau*

*1077 Ray W. Herrick Laboratories, School of Mechanical Engineering, Purdue University, West Lafayette, IN 47907-1077, USA*

Received 15 October 2001; accepted 1 May 2002

**Abstract**

The purpose of this study was to develop a theoretical model for the flow-induced vibration of viscoelastically supported rectangular plates. In particular, the influence of the dynamic mechanical properties of the elements supporting the plate was investigated. The case of a homogeneous rectangular plate supported along all four edges by a complex viscoelastic element was treated. The Rayleigh–Ritz method was used applying beam functions as the trial functions. This approach ensured a fast convergence rate, which is advantageous for vibration analysis of high order modes. The flow-induced vibration of the plate was calculated using the Corcos model for the surface pressure loading. The results suggest that there is an optimal support stiffness that minimizes the flow-induced vibration response of the plate.


## 1. Introduction

Flow-induced structural vibrations are encountered in many practical engineering problems. For example, the side-glass window panels of road vehicles may be excited by turbulent flows when the vehicle is operated at cruise. This phenomenon is responsible for sound radiated inside the vehicle, a primary source of aerodynamic broadband noise [1]. In any situation where plates or panels are supported on one or several edges by compliant viscoelastic systems, such as in the case of flow-induced vibrations of side-glass windows supported by rubber seals (Fig. 1(a)), dissipation of vibration energy occurs mostly at the supports rather than within the structure itself [2,3]. In this case, the effects of the supporting elements on the vibration response of the plate determine the amplitude of the radiated sound.

*Corresponding author. Tel.: +1-765-494-9342; fax: +1-765-494-0787.
*E-mail address:* mongeau@ecn.purdue.edu (L. Mongeau).

0022-460X/03/$ - see front matter 
PII: S0022-460X(02)00955-0

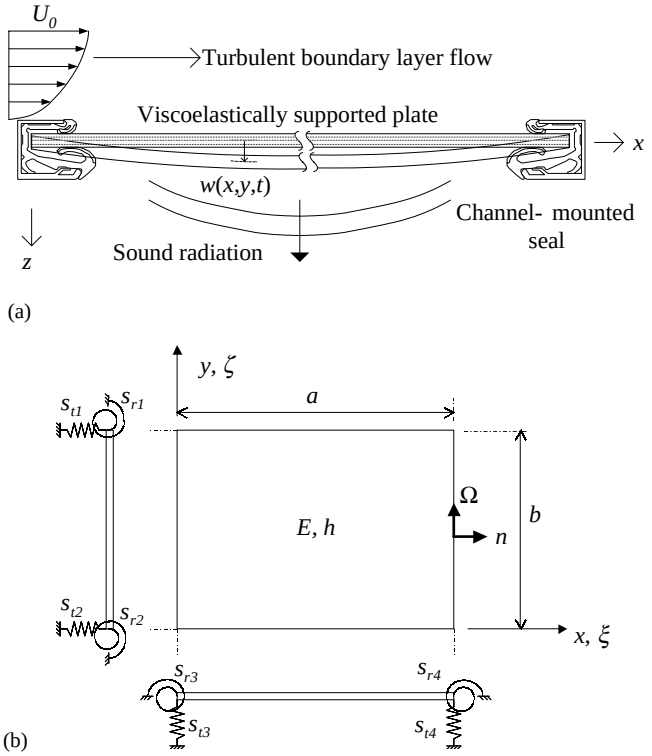


Fig. 1. (a) Sound radiation from flow-induced vibrations of a seal-supported rectangular plate. (b) Geometry of the rectangular plate and its boundary conditions. The supports are shown from a side view of the plate.

Flow-induced structural vibrations have been the objects of many previous studies [4–7]. Most studies of the flow-induced vibrations have been devoted to plates with geometric or natural boundary conditions. The problem of plates with general boundary conditions has been studied previously. Approximate methods based on the well-known Rayleigh–Ritz method have been used for a rectangular plate supported elastically on all four edges (general boundary conditions), for a discrete excitation [8]. The case of a similar structure excited by turbulent flow has been investigated using finite element and boundary element methods [9]. The Rayleigh–Ritz method has many advantages over numerical methods such as finite element and bounday element methods. It is less expensive, requires less computational effort, and thus it is more convenient for design optimization and parametric studies. It is limited, however, to structures with a simple geometry.

In the Rayleigh–Ritz method, the selection of the trial functions is important. Young [10] used beam functions as trial functions for the analysis of clamped and cantilevered plates. Berry et al. [11] considered two different sets of trial functions: Fourier series and polynomial functions. Fourier series, however, cannot accurately describe the response when there is a finite displacement at the boundary, a problem polynomial functions can remedy. Berry et al. accounted for the effects of the compliance of the support at the edges in their derivation of the

Hamiltonian of the system. Beslin and Nicolas [12] analyzed very high order plate bending modes by using two different trial function sets: hierarchical polynomials and hierarchical trigonometric functions. It was shown that hierarchical polynomials are inappropriate to predict very high order modes since the mass and stiffness matrices are often ill-conditioned because of numerical round-off errors. Hierarchical trigonometric functions yielded much better numerical stability compared to hierarchical polynomials.

The primary goal of the current investigation was to assess the influence of rubber seal properties on the flow-induced vibrations of side-glass window panels. The panels were idealized as rectangular homogeneous plates to allow for simple theoretical methods to be used. The energy dissipation mechanism was primarily associated with damping at the supports, in contrast with material damping of the panels themselves [3]. Such external damping mechanism may be easily controlled by changing the geometry or the material of the support. To analyze the effects of the support properties, the Rayleigh–Ritz method was used. Modified beam functions were used as the trial functions to minimize numerical errors at high frequencies. As discussed later, the use of beam functions ensured fast convergence and allowed the vibration analysis to be extended to high order modes.

The effects of support stiffness on the modal properties of the plate were investigated. The results for the first, the fourth, and the 20th modes were selected for discussion. The steady-state vibration response under a turbulent flow excitation was calculated. The Corcos wall pressure model was used. The effects of the support stiffness on the flow-induced vibration were investigated, in particular the velocity response at resonance.

## 2. Vibration analysis of A viscoelastically supported plate

### 2.1. Free vibration analysis

Fig. 1(a) illustrates one possible example of sound radiation from flow-induced vibrations of a viscoelastically supported plate. This configuration is intended to idealize a seal-supported vehicle side-glass window. One side of the plate is excited by a turbulent flow. The sound generated from the vibrations of the plate is radiated into the interior of the vehicle. Fig. 1(b) shows a schematic of the viscoelastically supported rectangular plate. A Cartesian co-ordinate system is used (Fig. 1). The plate has a uniform thickness, $h$, and dimensions $a \times b$. The normalized spatial coordinates, $\xi = x/a$ and $\zeta = y/b$, vary between 0 and 1. The motion of the four edges is restrained by translational and rotational springs. The plate is supported by translational springs with stiffnesses $s_{t1}, s_{t2}, s_{t3}$, and $s_{t4}$ along the boundaries at $y = 0$, $y = b$, $x = 0$, and $x = a$, respectively. Rotational springs with stiffness, $s_{r1}, s_{r2}, s_{r3}$, and $s_{r4}$ are arranged in a similar fashion.

A variational formulation, the Rayleigh–Ritz method, was used for the vibration analysis. The generalized coordinates were time-dependent. In this case, the Rayleigh–Ritz method is sometimes referred to in the literature as the assumed-modes method [13]. The kinetic, $T$, and potential energy, $V$, for transverse vibration of the plate was calculated using [11]:

$$T = \int_0^a \int_0^b \frac{1}{2}\rho h \left(\frac{\partial w}{\partial t}\right)^2 \mathrm{d}y\mathrm{d}x, \tag{1}$$

$$V = \int_0^a \int_0^b \frac{1}{2} D \left[ \left( \frac{\partial^2 w}{\partial x^2} \right)^2 + 2v \left( \frac{\partial^2 w}{\partial x^2} \right) \left( \frac{\partial^2 w}{\partial y^2} \right) + \left( \frac{\partial^2 w}{\partial y^2} \right)^2 + 2(1-v) \left( \frac{\partial^2 w}{\partial x \partial y} \right)^2 \right] \mathrm{d}y \, \mathrm{d}x + \int_\Omega \left[ \frac{1}{2} s_{tj} w^2 + \frac{1}{2} s_{rj} \left( \frac{\partial w}{\partial n} \right)^2 \right] \mathrm{d}\Omega \tag{2}$$

where $\Omega$ and $n$ are the contours and the normal direction (Fig. 1(b)) along the boundary of the plate, respectively, $D = Eh^3/12(1-v^2)$ is the bending stiffness of the rectangular plate, $w$ is the transverse displacement, $\rho$ is the density, $h$ is the thickness, $E$ is Young's modulus, and $v$ is the Poisson ratio. The contribution of the viscoelastic supports and their interaction with the plate vibrations is taken into account in the calculation of the potential energy, Eq. (2). The transverse displacement of the plate was approximated as

$$w(x, y, t) = \sum_{mn=1}^{N^2} \Gamma_{mn}(x, y) \alpha_{mn}(t), \tag{3}$$

where $\Gamma_{mn}$ are the trial functions chosen from a complete set, and $\alpha_{mn}$ are the generalized coordinates. Given the $N^2$-trial functions, the plate vibration response is approximated as an $N^2$-degrees-of-freedom discrete system. After substituting Eq. (3) into Eqs. (1) and (2), Lagrange's equations of motion,

$$\frac{\mathrm{d}}{\mathrm{d}t} \left( \frac{\partial L}{\partial \dot{\alpha}_{mn}} \right) - \frac{\partial L}{\partial \alpha_{mn}} = 0, \quad mn = 1, 2, \ldots, N^2, \tag{4}$$

were applied, where $L = T - V$ is the system Lagrangian. This yields a set of equations of motion

$$[M]\{\ddot{\alpha}\} + [K]\{\alpha\} = 0, \tag{5}$$

where $[M]$ and $[K]$ are the mass and stiffness matrices, respectively. In a normal mode analysis to calculate the mode shapes and natural frequencies, the solution of Eq. (5) was assumed to be

$$\alpha_{mn}(t) = \mathrm{Re}\{\hat{\alpha}_{mn} \mathrm{e}^{\mathrm{i}\omega t}\}, \tag{6}$$

where $\mathrm{i} = \sqrt{-1}$ and $\hat{\alpha}_{mn}$ is the complex amplitude of $\alpha_{mn}$. The following eigenvalue problem was obtained from Eqs. (5) and (6):

$$\{-\omega^2[M] + [\hat{K}]\}\{\hat{\alpha}\} = 0. \tag{7}$$

A commonly accepted method to model the dissipation of vibration energy is to use a complex stiffness for the dynamic properties of mechanical supports. In this study, the complex stiffnesses of the supports were defined

$$\hat{S}_{tj} = S_{tj}(1 + \mathrm{i}\eta_{tj}), \quad j = 1, \ldots, 4 \tag{8a}$$

$$\hat{S}_{rj} = S_{rj}(1 + \mathrm{i}\eta_{rj}), \quad j = 1, \ldots, 4 \tag{8b}$$

where $\eta_{tj}$ and $\eta_{rj}$ are the loss factors. Since the support stiffness is complex, the stiffness matrix in Eq. (7) is also complex. From Eq. (7), the natural frequencies of the plate, $\hat{\omega}_j$, and the associated eigenvectors, $\{\hat{V}_j\}$, were calculated. Note that the eigenvectors are orthogonal because the above mass and stiffness matrices are symmetric [13]. The calculated eigenvalues from Eq. (7), $\hat{\omega}_j$, are complex when the plate is supported viscoelastically. The damped natural frequencies, $f_j$, and the

system loss factors, $\eta_j$, are related to the complex eigenvalues through

$$\hat{\omega}_j = (2\pi f_j)\sqrt{1 + i\eta_j}. \tag{9}$$

The calculated eigenvectors were scaled to satisfy the following condition:

$$\{\hat{V}_j^*\}^T\{\hat{V}_m\} = \delta_{jm}, \tag{10}$$

where $\delta_{jm}$ is the Kronecker delta function and $\{\hat{V}_j^*\}$ is the complex conjugate of $\{\hat{V}_j\}$.

### 2.2. Trial functions

As mentioned in the introduction, the selection of trial functions in Eq. (3) determines the convergence rate and the accuracy of the solution. In this study, beam functions were used. In general, the trial functions for the transverse plate displacement are in the form

$$\Gamma_{mn}(\xi, \zeta) = \phi_m(\xi)\psi_n(\zeta), \tag{11}$$

where $\phi_m$ and $\psi_n$ are functions only of the $\xi$- and $\zeta$-coordinates, respectively. These functions satisfy the boundary conditions for one-dimensional transverse vibrations of the elastically supported plate, as illustrated in Fig. 2. To obtain $\phi_m$, the plate is assumed to vibrate only in the $\xi$-direction without any constrain in the $\zeta$-direction (one-dimensional response). In this case, the equation of motion is [14]

$$\frac{D}{a^4}\frac{\partial^4 w}{\partial \xi^4} + \rho h\frac{\partial^2 w}{\partial t^2} = 0. \tag{12}$$

Fig. 2 shows the elastic boundary conditions imposed in the $\xi$-direction. Note that the real part of the complex stiffnesses (in Eq. (8)) was used when applying the boundary conditions. Thus, the modal shape functions are purely real. The analysis procedures for one-dimensional vibrations of plates are exactly same as those for vibrating beams which is discussed for general boundary conditions in Ref. [2]. The shape functions usually consist of sine, cosine, hyperbolic sine, and hyperbolic cosine functions, i.e.,

$$\phi_m(\xi) = A_m \sin\beta_m\xi + B_m \cos\beta_m\xi + C_m' \sinh\beta_m\xi + D_m' \cosh\beta_m\xi, \tag{13}$$

where $\beta_m$ are the frequency parameters. In the present study, it was found that the use of hyperbolic functions caused numerical errors in calculating the shape functions. As discussed by Chen and Zhou [15], exponential waves affect the vibration response only at the boundaries and decay exponentially away from the boundary. When hyperbolic functions are used in the

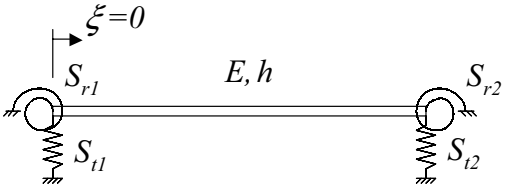


Fig. 2. Vibrating plate with elastic supports at the boundary. One-dimensional plane bending waves were assumed for the evaluation of the trial function coefficients.

numerical calculations, extremely small round-off errors are required to describe these exponential decaying waves for large value of the frequency parameters, $\beta_m$. The modified beam functions were therefore chosen to have the form

$$\phi_m(\xi) = A_m \sin \beta_m \xi + B_m \cos \beta_m \xi + C_m e^{\beta_m(\xi-1)} + D_m e^{-\beta_m \xi}. \tag{14}$$

In the above beam functions, $C_m$ and $D_m$ are the relative magnitudes of exponentially decaying wave at $\xi = 1$ and 0, respectively. The use of modified functions such as Eq. (14) minimizes round-off errors in the vibration response near the edges.

The plate displacement for one-dimensional transverse vibrations is

$$w(x,t) = \sum_{m=1}^{\infty} \phi_m(x)\alpha_m(t). \tag{15}$$

Boundary conditions, shown in Fig. 2, are as follows:

at $\xi = 0$,

$$\frac{\partial^3 \phi(0)}{\partial \xi^3} = -T_1 \phi(0), \tag{16a}$$

$$\frac{\partial^2 \phi(0)}{\partial \xi^2} = R_1 \frac{\partial \phi(0)}{\partial \xi}, \tag{16b}$$

at $\xi = 1$,

$$\frac{\partial^3 \phi(1)}{\partial \xi^3} = T_2 \phi(1), \tag{16c}$$

$$\frac{\partial^2 \phi(1)}{\partial \xi^2} = -R_2 \frac{\partial \phi(1)}{\partial \xi} \tag{16d}$$

where the non-dimensional stiffness parameters are defined as

$$T_j = S_{tj} a^3 / D, \tag{17a}$$

$$R_j = S_{rj} a / D, \quad j = 1, 2. \tag{17b}$$

Substituting the beam functions into Eq. (16) results in a set of four homogeneous equations, expressed in matrix form as follows:

$$\begin{bmatrix} -\beta_m^3 & T_1 & (T_1 + \beta_m^3)e^{-\beta_m} & T_1 - \beta_m^3 \\ R_1 & \beta_m & (R_1 - \beta_m)e^{-\beta_m} & -R_1 - \beta_m \\ T_2 \sin \beta_m + \beta_m^3 \cos \beta_m & T_2 \cos \beta_m - \beta_m^3 \sin \beta_m & T_2 - \beta_m^3 & (T_2 + \beta_m^3)e^{-\beta_m} \\ R_2 \cos \beta_m - \beta_m \sin \beta_m & -R_2 \sin \beta_m - \beta_m \cos \beta_m & R_2 + \beta_m & (-R_2 + \beta_m)e^{-\beta_m} \end{bmatrix} \begin{Bmatrix} A_m \\ B_m \\ C_m \\ D_m \end{Bmatrix} = \begin{Bmatrix} 0 \\ 0 \\ 0 \\ 0 \end{Bmatrix}. \tag{18}$$

Eq. (18) is an eigenvalue problem. The roots, $\beta_m$, that make the $4 \times 4$ matrix singular were calculated and the beam function coefficients, $A_m$, $B_m$, $C_m$, and $D_m$, were obtained from the corresponding eigenvectors. The resulting beam functions are orthogonal. They were normalized to satisfy the conditions

$$\int_0^1 \phi_m(\xi)\phi_p(\xi)\,\mathrm{d}\xi = \delta_{mp}. \tag{19}$$

Similar conditions are also satisfied by the shape functions along the $\zeta$-direction, $\psi_n$, which were calculated following the same procedures as for $\phi_m$. Consequently, the trial functions, $\Gamma_{mn}$, satisfy the following orthogonal conditions:

$$\int_0^1 \int_0^1 \Gamma_{mn}(\xi,\zeta)\Gamma_{pq}(\xi,\zeta)\,\mathrm{d}\xi\,\mathrm{d}\zeta = \delta_{mp}\delta_{nq}. \tag{20}$$

The beam functions were transformed into the following form to minimize the number of integrations necessary in the evaluation of the mass and stiffness matrices:

$$\phi_m(\xi) = \Lambda_m \sin\left(\beta_m\xi + \varphi_m\right) + C_m \mathrm{e}^{\beta_m(\xi-1)} + D_m \mathrm{e}^{-\beta_m\xi}, \tag{21}$$

where

$$\Lambda_m = \sqrt{A_m^2 + B_m^2}, \tag{22a}$$

$$\varphi_m = \tan^{-1} B_m/A_m. \tag{22b}$$

In Eq. (21), the trial functions consist of sinusoidal and exponential functions. Generally, the source of ill-conditioned mass and stiffness matrices is the increasing round-off errors as the order of the trial functions increases. When polynomials are used as trial functions, very high order polynomials can result in large round-off errors due to the large values of the polynomial coefficients and the limited dynamic range of computer memory [12]. For beam functions such as those shown in Eq. (21), round-off errors do not increase as the order of the trial function increases, which is a significant advantage for the analysis of high order modes.

### 2.3. Mass and stiffness matrices

The mass and stiffness matrices were calculated using the trial functions defined in Eq. (11). The coefficients are

$$M_{mnpq} = (\rho hab)\delta_{mp}\delta_{nq}, \tag{23}$$

$$\begin{aligned}\hat{K}_{mnpq} = {} & D\left[\frac{b}{a^3}\delta_{nq}X2_{mp} + \frac{a}{b^3}\delta_{mp}Y2_{nq} + \frac{\nu}{ab}\left(X1_{mp}Y1_{nq} + X1_{pm}Y1_{qn}\right) + \frac{2(1-\nu)}{ab}X3_{mp}Y3_{nq}\right] \\ & + a\delta_{mp}\left[\hat{S}_{t1}\psi_n(0)\psi_q(0) + \hat{S}_{t2}\psi_n(1)\psi_q(1)\right] + b\delta_{nq}\left[\hat{S}_{t3}\phi_m(0)\phi_p(0) + \hat{S}_{t4}\phi_m(1)\phi_p(1)\right] \\ & + \frac{a}{b^2}\delta_{mp}\left[\hat{S}_{r1}\frac{\partial\psi_n}{\partial\zeta}(0)\frac{\partial\psi_q}{\partial\zeta}(0) + \hat{S}_{r2}\frac{\partial\psi_n}{\partial\zeta}(1)\frac{\partial\psi_q}{\partial\zeta}(1)\right] \\ & + \frac{b}{a^2}\delta_{nq}\left[\hat{S}_{r3}\frac{\partial\phi_m}{\partial\xi}(0)\frac{\partial\phi_p}{\partial\xi}(0) + \hat{S}_{r4}\frac{\partial\phi_m}{\partial\xi}(1)\frac{\partial\phi_p}{\partial\xi}(1)\right],\end{aligned} \tag{24}$$

where $X1_{mp}$, $X2_{mp}$, $X3_{mp}$, $Y1_{nq}$, $Y2_{nq}$ and $Y3_{nq}$ are defined as

$$X1_{mp} = \int_0^1 \phi_m \frac{\partial^2 \phi_p}{\partial \xi^2} \, d\xi, \tag{25a}$$

$$X2_{mp} = \int_0^1 \frac{\partial^2 \phi_m}{\partial \xi^2} \frac{\partial^2 \phi_p}{\partial \xi^2} \, d\xi, \tag{25b}$$

$$X3_{mp} = \int_0^1 \frac{\partial \phi_m}{\partial \xi} \frac{\partial \phi_p}{\partial \xi} \, d\xi, \tag{25c}$$

$$Y1_{nq} = \int_0^1 \psi_n \frac{\partial^2 \psi_q}{\partial \zeta^2} \, d\zeta, \tag{26a}$$

$$Y2_{nq} = \int_0^1 \frac{\partial^2 \psi_n}{\partial \zeta^2} \frac{\partial^2 \psi_q}{\partial \zeta^2} \, d\zeta, \tag{26b}$$

$$Y3_{nq} = \int_0^1 \frac{\partial \psi_n}{\partial \zeta} \frac{\partial \psi_q}{\partial \zeta} \, d\zeta. \tag{26c}$$

The evaluation of these integrals was performed using three integral formulas shown in Appendix A.

### 2.4. Verification of the method

By adjusting the stiffness of the translational and rotational springs, the Rayleigh–Ritz method described in the previous sections can be applied to analyze the vibration of plates with arbitrary boundary conditions. In the following simulations, the stiffness of the supports was assumed to be uniform along the boundary of the plate. The translational springs in Fig. 1(b) have a uniform complex stiffness of $\hat{S}_{tj} = S_t(1 + i\eta_t)$, and the rotational springs have a constant complex stiffness of $\hat{S}_{rj} = S_r(1 + i\eta_r)$ . Internal energy dissipation within the plate itself was assumed to be negligible. The plate properties were chosen to be: $a = 0.466\,\text{m}$; $b = 0.375\,\text{m}$; $h = 0.00338\,\text{m}$; $\rho = 2700\,\text{kg/m}^3$; $E = 7.2 \times 10^{10}\,\text{Pa}$; and $v = 0.34$.

Fig. 3 shows plots of a few trial functions defined in Equation (21) for a plate supported by translational springs only. The first and second trial functions ($m = 1,2$) were selected for presentation. The trial function shapes are similar to the mode shapes of simply supported beams when the translational stiffness is large ($\sim 10^{10}$ Pa). As the translational stiffness is decreased, the trial function shapes approach the mode shapes of free–free beams. In particular, the first and second trial function shapes approach the mode shapes of translational and rocking rigid body modes. In between these two extreme cases, the trial function shapes gradually change from the mode shapes of a simply supported beam to those of a free–free beam as the translational stiffness is decreased.

To verify the analytical model, and the accuracy of predictions using beam trial functions, the natural frequencies predicted using three different methods were compared, as shown in Tables 1 and 2. Table 1 shows results for a simply supported plate. A closed form expression for the natural

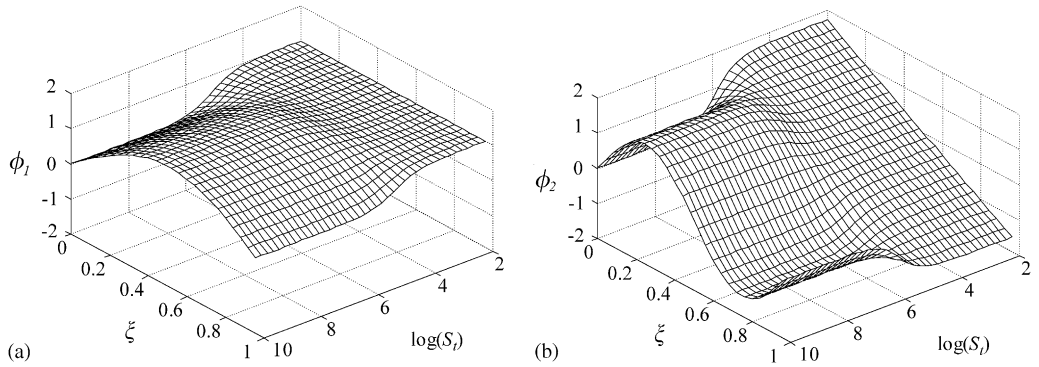


Fig. 3. Variation of the trial function in the $x$-direction with the support stiffness, $S_t$. (a) First ($m = 1$) and (b) second ($m = 2$) trial function. $S_r = 0$.

Table 1
Comparison between natural frequencies of a simply supported plate predicted using different methods

| Mode number | Eq. (27) | Beam functions set |
|---|---|---|
| 1 | 98.60271 | 98.60271 |
| 2 | 214.8694 | 214.8694 |
| 3 | 278.1441 | 278.1441 |
| 4 | 394.4109 | 394.4109 |
| 5 | 408.6473 | 408.6473 |
| 6 | 577.3799 | 577.3799 |
| 7 | 588.1887 | 588.1887 |
| 8 | 679.9363 | 679.9363 |
| 9 | 693.6466 | 693.6466 |
| 10 | 859.4777 | 859.4777 |

Table 2
Comparison between natural frequencies and system loss factors of a viscoelastically supported plate

| Mode number | Polynomial functions set [11] | | Beam functions set | |
|---|---|---|---|---|
| | $f_j$ | $\eta_j$ | $f_j$ | $\eta_j$ |
| 1 | 87.38673 | 0.02835 | 87.54528 | 0.02768 |
| 2 | 178.0804 | 0.04260 | 178.4281 | 0.04159 |
| 3 | 221.3751 | 0.05580 | 221.6634 | 0.05522 |
| 4 | 286.873 | 0.06494 | 287.8409 | 0.06321 |
| 5 | 306.2211 | 0.06845 | 306.6278 | 0.06774 |
| 6 | 381.1667 | 0.08786 | 381.4951 | 0.08745 |
| 7 | 390.8103 | 0.07703 | 392.1302 | 0.07540 |
| 8 | 425.8642 | 0.08925 | 427.0692 | 0.08755 |
| 9 | 452.6486 | 0.07984 | 453.2667 | 0.07932 |
| 10 | 518.4296 | 0.07971 | 520.3834 | 0.07778 |

frequencies of the simply supported plate is

$$f_{mn} = \left[\left(\frac{m}{a}\right)^2 + \left(\frac{n}{b}\right)^2\right]\sqrt{\frac{\pi^2 D}{4\rho h}}. \tag{27}$$

For the Rayleigh–Ritz solution, the boundary conditions were enforced by assigning $\hat{S}_t$ a large value, $10^{10}$ Pa, and $\hat{S}_r = 0$. Good agreement was obtained between the results for the two different methods.

Table 2 shows the predicted natural frequencies for one viscoelastically supported plate. The boundary stiffnesses were chosen to be: $\hat{S}_t = 2.2 \times 10^6(1 + \mathrm{i}\,0.15)$ Pa; $\hat{S}_r = 0$. In this case, the predicted resonance frequencies were similar to measured values [3]. The trial function shapes are different from the mode shapes of the simply supported or free–free beam (Fig. 3). The results were compared to those of another numerical study by Berry et al. [11] who used polynomial functions as trial functions, $\Gamma_{mn}(\xi, \zeta) = \xi^m \zeta^n$. In applying the method of Berry et al., the plate was discretized as a system with 196 degrees of freedom ($N = 14$). In the present study, the plate was approximated as a system with 81 degrees of freedom ($N = 9$). The differences between the natural frequencies predicted using the two methods were less than 1%.

Fig. 4 shows the convergence rates of the predicted plate natural frequencies obtained using the beam functions and the polynomial functions. The results converge to nearly the same value for each mode. The solutions converged faster with the beam functions because the beam functions are a better representation of the actual mode shapes.

In this study, the frequency range of interest ranged from 0 to 2000 Hz. As shown in Fig. 4, the predicted natural frequencies for the 49th and the 64th modes converged within less than 5% for $N = 9$. The natural frequencies of the 49th and 64th modes converged to 2200 and 3100 Hz, respectively. This suggests that the use of $N = 9$ did ensure the convergence of all modes with natural frequencies less than 2000 Hz.

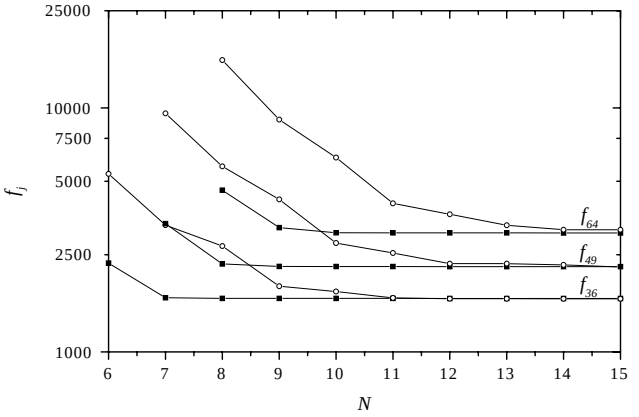


Fig. 4. Predicted variation of natural frequency with the order of the beam function ($N$). Comparison of results predicted using two different trial functions sets: —■—, beam functions; —○—, polynomial functions.

## 3. Response to random excitation

### 3.1. Flow-induced vibration

To calculate the flow-induced vibration response, the frequency transfer function between a harmonic excitation at one location and the resulting harmonic transverse displacement response at other location was used. This frequency transfer function was determined from the modal shape functions and the natural frequencies. The modal shape functions, $\hat{\Psi}_j$, were obtained from the eigenvalue problem, Eq. (8), using

$$\hat{\Psi}_j(\xi,\zeta) = \sum_{mn=1}^{N^2} \Gamma_{mn}(\xi,\zeta)\,\hat{V}_j(mn). \tag{28}$$

The transverse displacement is given in terms of the associated generalized coordinates $q_j(t)$ by (assuming harmonic vibrations of the plate, $q_j(t) = \mathrm{Re}\{\hat{q}_j e^{i\omega t}\}$)

$$w(\xi,\zeta,t) = \mathrm{Re}\{\sum_{j=1}^{N^2} \hat{\Psi}_j(\xi,\zeta)\hat{q}_j e^{i\omega t}\}. \tag{29}$$

From Eqs. (10), (20) and (28) the modal shape functions are orthogonal to each other, i.e.,

$$\int_0^1 \int_0^1 \hat{\Psi}_j(\xi,\zeta)\hat{\Psi}^*_m(\xi,\zeta)\,\mathrm{d}\xi\,\mathrm{d}\zeta = \delta_{jm}. \tag{30}$$

The equations of motion for the $N^2$-degree of freedom system are expressed as

$$\rho hab\left(-\omega^2 + \hat{\omega}_j^2\right)\hat{q}_j = \hat{f}_{\Psi_j}, \quad j = 1, \ldots, N^2 \tag{31}$$

where $\hat{f}_{\Psi_j}$ are the modal forces, given by the integrals

$$\hat{f}_{\Psi_j} = ab \int_0^1 \int_0^1 \hat{\Psi}_j(\xi,\zeta)p(\xi,\zeta)\,\mathrm{d}\xi\,\mathrm{d}\zeta. \tag{32}$$

Here $p$ is the external distributed pressure loading from the turbulent flow. The frequency response function between one applied point force at $\mathbf{s}_1$ and the associated transverse displacement at $\mathbf{s}_2$ is [16]

$$H(\mathbf{s}_1,\mathbf{s}_2,\omega) = \sum_{j=1}^{N^2} \hat{\Psi}_j(\mathbf{s}_1)\hat{\Psi}_j(\mathbf{s}_2)\hat{H}_j(\omega), \tag{33}$$

where $\hat{H}_j$ is the frequency response function for the generalized coordinate $q_j$, obtained from Eq. (31):

$$\hat{H}_j(\omega) = \frac{1}{\rho hab\left(-\omega^2 + \hat{\omega}_j^2\right)}. \tag{34}$$

The turbulent flow excitation is usually specified using the cross-spectral density of the wall pressure. The spatially averaged mean square velocity of the plate, $v_{av}$, is [16]

$$v_{av}(\omega) = \sum_{j=1}^{N^2} \left|\omega \hat{H}_j(\omega)\right|^2 \int_A \int_A \hat{\Psi}_j^*(\mathbf{s}_1)\hat{\Psi}_j(\mathbf{s}_2)\hat{G}_{pp}(\mathbf{s}_1, \mathbf{s}_2, \omega)\, \mathrm{d}\mathbf{s}_1\, \mathrm{d}\mathbf{s}_2, \tag{35}$$

where $\hat{G}_{pp}$ is the cross-spectral density of the wall pressure.

To estimate the flow-induced vibration of structures, the Corcos model is widely used due to its mathematical simplicity compared to other wall pressure models. In the Corcos model, the cross-spectral density of the wall pressure is assumed to have the form [4]

$$\hat{G}_{pp}(\xi_1, \xi_2, \zeta_1, \zeta_2, \omega) = \Phi_p(\omega) \mathrm{e}^{-\gamma_x|\omega a(\xi_2-\xi_1)/U_c|} \mathrm{e}^{-\gamma_y|\omega b(\zeta_2-\zeta_1)/U_c|} \mathrm{e}^{-\mathrm{i}\omega a(\xi_2-\xi_1)/U_c}, \tag{36}$$

where $\Phi_p$ is the wall pressure spectral density, $\xi_1$ and $\xi_2$ are the normalized locations along the streamwise direction, $\zeta_1$ and $\zeta_2$ are the normalized locations along the spanwise direction. The parameters $\gamma_x$ and $\gamma_y$ are the decay rates related to the coherence in the streamwise and the spanwise directions, respectively, and $U_c$ is the convection speed of "frozen" turbulent eddies near the wall. The coherence functions are assumed to have an exponential form. Since it is difficult to perform the integration directly in Eq. (35), the equation was rewritten after replacing $\hat{G}_{pp}$ with Eq. (36) as (after some algebra)

$$v_{av}(\omega) = (2ab)^2 \Phi_p(\omega) \sum_{j=1}^{N^2} \left|\omega \hat{H}_j(\omega)\right|^2 \mathrm{Re}\left\{ \int_0^1 \int_0^1 \hat{\Psi}_j^*(\xi_1, \zeta_1) \mathrm{e}^{\frac{-(\gamma_x+\mathrm{i})\omega a}{U_c}\xi_1} \mathrm{e}^{\frac{-\gamma_y \omega b}{U_c}\zeta_1} \right.$$
$$\left. \left[ \int_0^{\zeta_1} \int_0^{\xi_1} \hat{\Psi}_j(\xi_2, \zeta_2) \mathrm{e}^{\frac{-(\gamma_x+\mathrm{i})\omega a}{U_c}\xi_2} \mathrm{e}^{\frac{-\gamma_y \omega b}{U_c}\zeta_2}\, \mathrm{d}\xi_2 \mathrm{d}\zeta_2 \right] \mathrm{d}\xi_1\, \mathrm{d}\zeta_1 \right\}, \tag{37}$$

which is more convenient to integrate. From Eqs (28) and (37), the spatially averaged mean square velocity of the plate is

$$v_{av}(\omega) = \sum_{j=1}^{N^2} \left|\omega \hat{H}_j(\omega)\right|^2 I_j(\omega), \tag{38}$$

where $I_j$ is defined as

$$I_j(\omega) = (2ab)^2 \Phi_p(\omega) \mathrm{Re}\left\{ \sum_{mn=1}^{N^2} \sum_{pq=1}^{N^2} \hat{V}_j^*(mn) \hat{V}_j(pq) \hat{T}_{mp}^{\xi} \hat{T}_{nq}^{\zeta} \right\}. \tag{39}$$

The frequency dependent functions $\hat{T}_{mp}^{\xi}$ and $\hat{T}_{nq}^{\zeta}$ were determined from the trial functions and the parameters of the Corcos model using

$$\hat{T}_{mp}^{\xi} = \int_0^1 \phi_m(\xi_1) \mathrm{e}^{\frac{-(\gamma_x+\mathrm{i})\omega a}{U_c}\xi_1} \left[ \int_0^{\xi_1} \phi_p(\xi_2) \mathrm{e}^{\frac{(\gamma_x+\mathrm{i})\omega a}{U_c}\xi_2}\, \mathrm{d}\xi_2 \right] \mathrm{d}\xi_1, \tag{40a}$$

$$\hat{T}_{nq}^{\zeta} = \int_0^1 \psi_n(\zeta_1) \mathrm{e}^{\frac{-\gamma_y \omega b}{U_c}\zeta_1} \left[ \int_0^{\zeta_1} \psi_q(\zeta_2) \mathrm{e}^{\frac{\gamma_y \omega b}{U_c}\zeta_2}\, \mathrm{d}\zeta_2 \right] \mathrm{d}\zeta_1, \tag{40b}$$

The integrations in Eq. (40) were performed analytically, as shown in Appendix B.

### 3.2. Approximation of the wall pressure spectrum

Although the Corcos model is relatively simple compared to other wall pressure models, the evaluation of the structural response using Eq. (38) is still rather complicated. Maidanik [17] proposed a simpler approach using delta functions as the correlation functions for the convecting and decaying pressure fields. The convection velocity then appears as a parameter in the delta functions. The Corcos wall pressure cross-spectral density mode, $\hat{G}_{pp}$, was approximated yielding the approximate form, $G'_{pp}$, given by

$$G'_{pp}(\xi_1, \xi_2, \zeta_1, \zeta_2, \omega) = C_\omega \Phi_p(\omega)\delta(\xi_1 - \xi_2)\delta(\zeta_1 - \zeta_2). \tag{41}$$

The approximate cross-spectral density, $G'_{pp}$, should yield the same characteristic spatial extent as the Corcos model. This condition can be expressed as

$$\int_{-\infty}^{\infty}\int_{-\infty}^{\infty}\int_{-\infty}^{\infty} G'_{pp}(\mu_\xi, \mu_\zeta, \omega)\,\mathrm{d}\mu_\xi\,\mathrm{d}\mu_\zeta\,\mathrm{d}\omega = \int_{-\infty}^{\infty}\int_{-\infty}^{\infty}\int_{-\infty}^{\infty} \hat{G}_{pp}(\mu_\xi, \mu_\zeta, \omega)\,\mathrm{d}\mu_\xi\,\mathrm{d}\mu_\zeta\,\mathrm{d}\omega. \tag{42}$$

where $\mu_\xi = \xi_1 - \xi_2$ and $\mu_\zeta = \zeta_1 - \zeta_2$, are streamwise and spanwise separations, respectively. Eq. (42) is satisfied when the approximate cross-spectral density is given as

$$G'_{pp}(\xi_1, \xi_2, \zeta_1, \zeta_2, \omega) = \frac{4\gamma_x U_c^2}{\omega^2\gamma_y(\gamma_x^2 + 1)}\Phi_p(\omega)\delta(\xi_1 - \xi_2)\delta(\zeta_1 - \zeta_2). \tag{43}$$

Inserting the above approximation into Eq. (35) leads to a simplified expression for the spatially averaged mean square velocity:

$$v_{av}(\omega) = \frac{4ab\gamma_x U_c^2}{\omega^2\gamma_y(\gamma_x^2 + 1)}\Phi_p(\omega)\sum_{j=1}^{N^2}\left|\omega\hat{H}_j(\omega)\right|^2. \tag{44}$$

When delta functions are used as correlation functions, the neighboring pressure fluctuations are assumed to be perfectly uncorrelated. Thus, the approximation shown in Eq. (44) is valid only when the decay rates are sufficiently large (i.e., $\gamma_x$, $\gamma_y > 0.1$). The Corcos model is known to successfully describe pressure fields under separated/reattached flows, which feature large decay rates [7]. The above approximation is valid for such pressure fields.

## 4. Results and discussion

### 4.1. Flow-induced vibration response

The predicted mean square velocity responses obtained using the Corcos model and its approximate form are shown in Fig. 5. The parameters of the Corcos model were selected to be: $U_c = 29$ m/s, $\gamma_x = 0.3$ and $\gamma_y = 0.7$ after Han et al. [7]. For all cases discussed in this paper, it was assumed that the wall pressure spectral density ($\Phi_p$) was unity over the entire frequency range. As shown in Fig. 5, the Corcos model and its approximate form yield essentially similar results, except for an overestimation of the response obtained from the delta function formulation at frequencies less than 30 Hz.

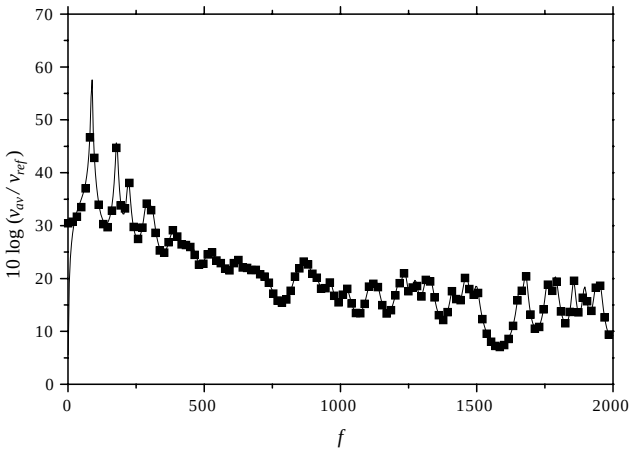


Fig. 5. Comparison between the spatially averaged velocity of the plate calculated using two different wall pressure models:, ■ the delta function model; ——, the Corcos model. $\gamma_x = 0.3$, $\gamma_y = 0.7$, $\hat{S}_t = 2.2 \times 10^6(1 + \mathrm{i}\,0.15)$ Pa, and $\hat{S}_r = 0$.

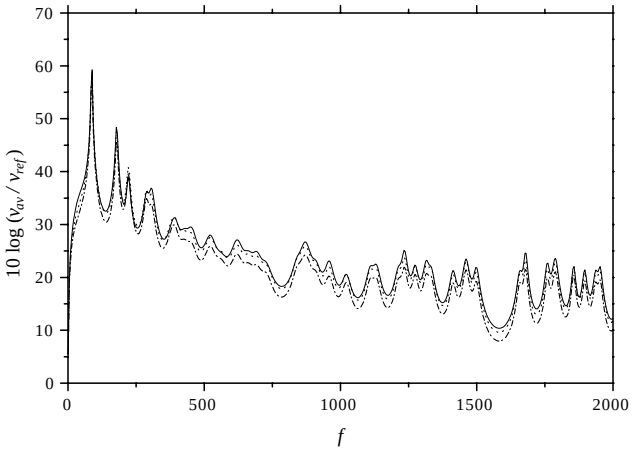


Fig. 6. Effects of decay rates on spatially averaged mean square velocity excited by convecting turbulent flows. The decay rates of the Corcos model: –.–.–, $\gamma_x = 1.0$ and $\gamma_y = 1.0$; – – – –, $\gamma_x = 0.6$ and $\gamma_y = 0.6$; —, $\gamma_x = 0.2$ and $\gamma_y = 0.2$. $\hat{S}_t = 2.2 \times 10^6(1 + \mathrm{i}\,0.15)$ Pa and $\hat{S}_r = 0$.

Fig. 6 shows the effects of the decay rates, $\gamma_x$ and $\gamma_y$, on the velocity response of the plate calculated from Eq. (38). A three-fold reduction in the decay rate value did not change the structural response significantly. This trend is consistent with Eq. (44) which shows that such change in decay rates increases the structural response by less than 1 dB. Graham [6] discussed the influence of convection speed on the radiated sound power from flow-excited plates. Eq. (44) shows that the vibration response is proportional to the square of the convection speed, corresponding to a 6 dB increase per doubling of the convection speed assuming that the wall

pressure spectra stays constant. The convection speed is thus an important parameter for accurate predictions of the flow-induced vibrations.

Fricke and Stevenson [18] showed experimentally that the amplitude of the wall pressure spectra increases approximately as the fourth power of the free stream flow velocity ($\Phi_p \propto U_0^4$). The convection velocity, $U_c$, is proportional to the free stream flow velocity, $U_0$ [7]. Taking this into account in Eq. (44), the flow-induced vibration amplitude is proportional to the sixth power of the convection velocity ($v_{av} \propto U_c^6$). The vibration amplitude increases rapidly with flow velocity. This result supports the well-known observation that vehicle interior aerodynamic noise, often dominated by flow-induced panel vibrations (in absence of aspiration), increases approximately as the sixth power of the vehicle velocity [1].

### 4.2. *Effects of support stiffness*

The effects of the support stiffness on the modal properties of the plate were investigated. The loss factors, $\eta_t$ and $\eta_r$, were assumed to be 0.15, independently of $S_t$ and $S_r$. The damped natural frequencies and the system loss factors for three specific modes, namely the first, fourth, and 20th modes, are shown in Figs. 7, 8, and 9 respectively. The first mode, shown in Fig. 7, features a rigid body mode with a natural frequency close to zero for values of $S_t$ near zero. The rigid body mode properties are independent of $S_r$. When the rigid body mode occurs, the system loss factor approaches that of the translational spring. Similar trends were also observed in the study by Kang and Kim [2].

For all modes, the natural frequencies change from those of freely supported plates to those of simply supported plates as $S_t$ is increased, and $S_r$ is maintained at zero. The natural frequencies change from those of simply supported plates to those of clamped plates when $S_r$ is increased and $S_t$ is large. With the exception of the first mode, the system loss factor reaches a maximum for unique values of $S_t$ and $S_r$ (Figs. 8 and 9). The maximum occurs at $S_t \cong 10^6$ Pa and $S_r \cong 10^3$ N/rad for the forth mode, and larger values of $S_t$ and $S_r$ for the 20th mode. The values of $S_t$ and $S_r$ corresponding to the maximum system loss factor increased as the mode number was increased.

The spatially averaged mean square velocity for a convecting wall pressure excitation, calculated from Eq. (38), is shown as a function of support stiffness in Figs. 10 and 11. Fig. 10

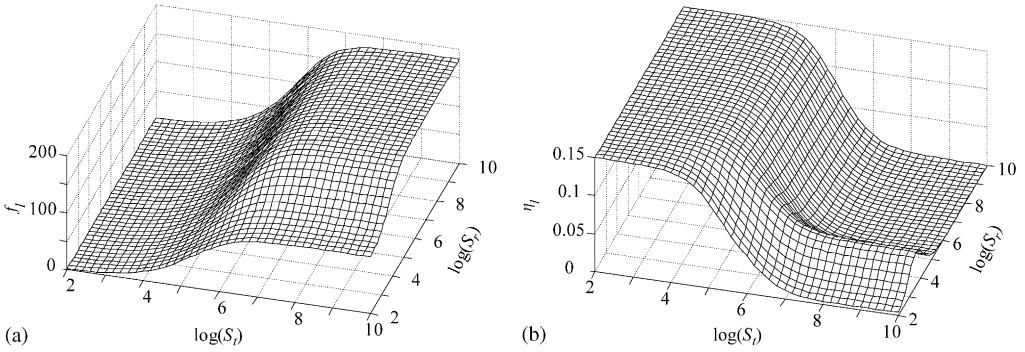


Fig. 7. Modal parameters vs. support stiffness for the first mode: (a) damped natural frequency, $f_1$; (b) system loss factor, $\eta_1$.

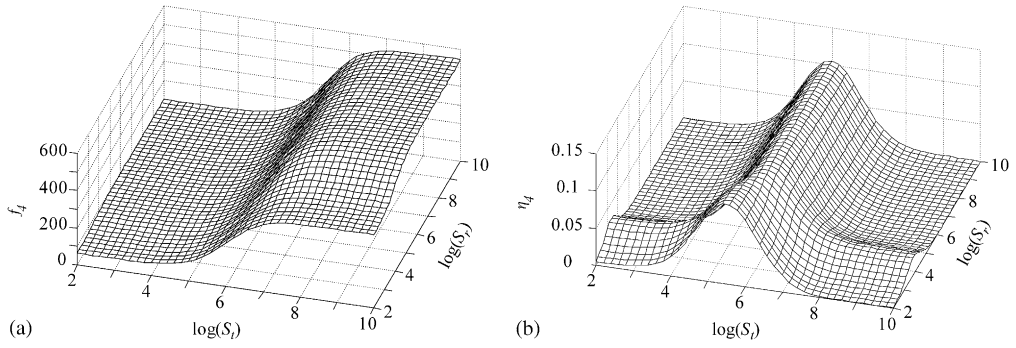


Fig. 8. Modal parameters vs. support stiffness for the fourth mode: (a) damped natural frequency, $f_4$ ; (b) system loss factor, $\eta_4$.

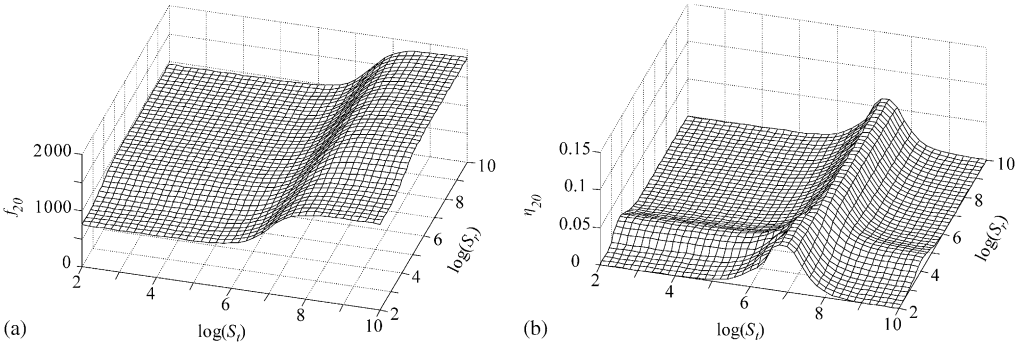


Fig. 9. Modal parameters vs. support stiffness for the 20th mode: (a) damped natural frequency, $f_{20}$ ; (b) system loss factor, $\eta_{20}$.

shows the influence of the translational stiffness, $S_t$, for $S_r = 0$. The support properties strongly influence the resonance frequencies. The resonance frequencies change from those of freely supported plates to those of simply supported plates as $S_t$ is increased. Fig. 11 shows the influence of the rotational stiffness, $S_r$, for $S_t = 100$. To prevent the rigid body modes of zero natural frequency, the translational stiffness was not set as zero. The resonance frequencies change from those of freely supported plates to those of guided plates as $S_r$ is increased. In both Figs. 10 and 11, the velocity response was found to be minimal for intermediate values of the complex stiffnesses. The amplitude of the minimum in the velocity response was lower for the plate supported by translation springs than for that supported by rotational spring. This suggests that restricting the translational motion may be more effective than restricting the rotational motion in controlling the vibration response amplitude. Small vibration amplitudes are accompanied by increased vibration energy dissipation at the boundary, and presumably minimal sound radiation. A systematic investigation of the optimal support stiffness to minimize the forced vibration of plates was performed by the authors, as described in a separate paper [19].

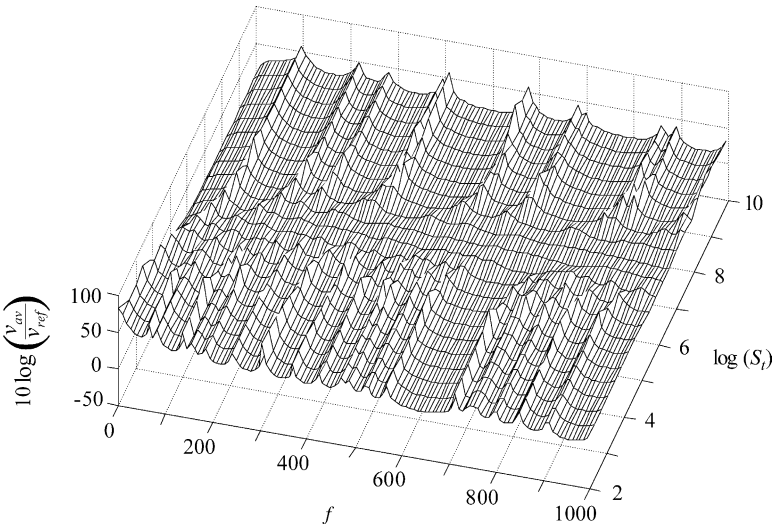


Fig. 10. Spatially averaged mean square velocity versus. translational spring stiffness. $\gamma_x = 0.3$, $\gamma_y = 0.7$, $\hat{S}_t = S_t(1 + \mathrm{i}\ 0.15)$, and $\hat{S}_r = 0$.

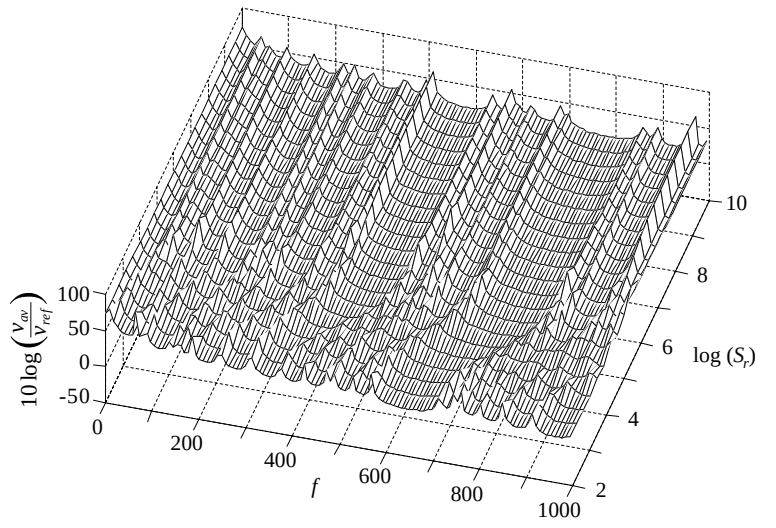


Fig. 11. Spatially averaged mean square velocity vs. rotational spring stiffness. $\gamma_x = 0.3$, $\gamma_y = 0.7$, $\hat{S}_t = 0$, and $\hat{S}_r = S_r(1 + \mathrm{i}\ 0.15)$.

## 5. Conclusions

The Rayleigh–Ritz method was applied to analyze the response of viscoelastically supported rectangular plates. Modified beam functions were used as the trial functions. The energy dissipated by the viscoelastic supports was taken into consideration using complex stiffnesses for

the translational and rotational springs at the rectangular plate boundaries. The use of the beam functions as the trial functions was found to ensure rapid convergence and yielded accurate solutions. The effects of the support stiffness on the modal properties of the plate were investigated. There are support stiffness values at which the system loss factors are maximum. These stiffness values are not the same between different modes and increase as the mode number. The effects from rotational and translational stiffness on the system loss factor were almost independent to each other.

The plate response excited by a turbulent flow was calculated. The Corcos model of the wall pressure correlation function was used. It was shown that the convection speed affected the flow-induced vibration more significantly than the decay rates. Optimal support stiffnesses were found that maximized the system loss factor and consequently minimized the forced vibration response of the plate. The translational springs attached at the edges were more effective than rotational springs in dissipating vibration energy. The model can be used to determine the optimal support dynamic mechanical properties for minimal sound transmission.

## Appendix A. Integral formulas

$$\int_0^1 \sin(\beta_1\xi+\varphi_1)\sin(\beta_2\xi+\varphi_2)\,\mathrm{d}\xi = \frac{1}{2}\left\{\frac{1}{\beta_1-\beta_2}[\sin(\beta_1-\beta_2+\varphi_1-\varphi_2)-\sin(\varphi_1-\varphi_2)] - \frac{1}{\beta_1+\beta_2}[\sin(\beta_1+\beta_2+\varphi_1+\varphi_2)-\sin(\varphi_1+\varphi_2)]\right\}, \quad (A.1)$$

$$\int_0^1 \sin(\beta_1\xi+\varphi_1)\mathrm{e}^{\beta_2\xi+\varphi_2}\,\mathrm{d}\xi = \frac{1}{\beta_1^2+\beta_2^2}\{\beta_1[\cos(\varphi_1)\mathrm{e}^{\varphi_2}-\cos(\beta_1+\varphi_1)\mathrm{e}^{\beta_2+\varphi_2}] + \beta_2[\sin(\beta_1+\varphi_1)\mathrm{e}^{\beta_2+\varphi_2}-\sin(\varphi_1)\mathrm{e}^{\varphi_2}]\}, \quad (A.2)$$

$$\int_0^1 \mathrm{e}^{\beta_1\xi+\varphi_1}\mathrm{e}^{\beta_2\xi+\varphi_2}\,\mathrm{d}\xi = \frac{1}{\beta_1+\beta_2}(\mathrm{e}^{\beta_1+\varphi_1+\beta_2+\varphi_2}-\mathrm{e}^{\varphi_1+\varphi_2}). \quad (A.3)$$

## Appendix B. Evaluation of $\hat{T}^{\xi}_{mp}$ and $\hat{T}^{\zeta}_{nq}$

The evaluation of $\hat{T}^{\xi}_{mp}$ and $\hat{T}^{\zeta}_{nq}$ was performed using the following integral formula:

$$\int_0^1 \phi_m(\xi_1)\mathrm{e}^{-\gamma\xi_1}\left[\int_0^{\xi_1}\phi_p(\xi_2)\mathrm{e}^{\gamma\xi_2}\,\mathrm{d}\xi_2\right]\mathrm{d}\xi_1$$

$$
\begin{aligned}
&= \frac{D_n}{\beta_n - \gamma} \int_0^1 [\Lambda_m \sin(\beta_m \xi + \varphi_m) + C_m e^{\beta_m(\xi-1)} + D_m e^{-\beta_m \xi}](e^{-\gamma\xi} - e^{-\beta_n \xi})\, d\xi \\
&\quad + \left\{ \frac{\Lambda_n}{\beta_n^2 + \gamma^2} [\beta_n \cos(\varphi_n) - \gamma \sin(\varphi_n)] - \frac{C_n}{\beta_n + \gamma} e^{-\beta_n} \right\} \\
&\quad \times \left\{ \int_0^1 [\Lambda_m \sin(\beta_m \xi + \varphi_m) + C_m e^{\beta_m(\xi-1)} + D_m e^{-\beta_m \xi}] e^{-\gamma\xi}\, d\xi \right\} \\
&\quad + \int_0^1 [\Lambda_m \sin(\beta_m \xi + \varphi_m) + C_m e^{\beta_m(\xi-1)} + D_m e^{-\beta_m \xi}] \\
&\quad \times \left\{ \frac{\Lambda_n}{\beta_n^2 + \gamma^2} [-\beta_n \cos(\beta_n \xi + \varphi_n) + \gamma \sin(\beta_n \xi + \varphi_n)] + \frac{C_n}{\beta_n + \gamma} e^{\beta_n(\xi-1)} \right\} d\xi. \qquad \text{(B.1)}
\end{aligned}
$$

The integrations in the above equation were evaluated using the integral formulas in Appendix A.

## Appendix C. Nomenclature

| | |
|---|---|
| $a, b$ | plate dimensions in $x$ and $y$ directions (m) |
| $A_m, B_m, C_m, D_m, \Lambda_m$ | beam function coefficients |
| $\alpha_{mn}$, $\hat{q}_j$ | generalized co-ordinates |
| $D$ | bending stiffness of plate (N · m) |
| $E$ | elastic modulus (Pa) |
| $f$ | frequency (Hz) |
| $f_j$ | damped natural frequency of jth mode (Hz) |
| $\hat{f}_{\Psi_j}$ | modal force of $j$th mode (N) |
| $h$ | plate thickness (m) |
| $\hat{H}_j$ | frequency response function in terms of generalized co-ordinates |
| $[\hat{K}]$ | modal stiffness matrix (N/m) |
| $L$ | system Lagrangian (J) |
| $[M]$ | modal mass matrix (kg) |
| $p$ | distributed pressure excitation (Pa) |
| $\mathbf{s}_1, \mathbf{s}_2$ | position vector on plate surface |
| $\hat{G}_{pp}$ | wall pressure cross-spectral density ($Pa^2$/Hz) |
| $\hat{S}_r$, $\hat{S}_t$ | complex stiffness of rotational (N/rad) and translational spring (Pa) |
| $T$ | kinetic energy of plate (J) |
| $W$ | transverse displacement of plate (m) |
| $U_c$ | convection velocity (m/s) |
| $v_{av}$ | spatially averaged mean square velocity of plate ($m^2/s^2$/Hz) |
| $v_{\text{ref}}$ | reference mean square velocity, $10^{-12}\, m^2/s^2$ |
| $V$ | potential energy of the plate (J) |
| $\hat{V}_j$ | $j$th eigenvector of plate |

| | |
|---|---|
| $\Omega$ | contour along the boundary of plate (m) |
| $\gamma_x, \gamma_y$ | decay rate in $x$ and $y$ directions |
| $\Gamma_{mn}$, $\hat{\Psi}_{mn}$ | trial functions of plate displacement |
| $\phi_m, \psi_n$ | beam functions in $x$ and $y$ directions |
| $\eta_j$ | system loss factor of $j$th mode |
| $\eta_R, \eta_T$ | loss factors of rotational and translational spring |
| $v$ | the Poisson ratio of plate |
| $\xi, \zeta$ | normalized spatial co-ordinate |
| $\mu_\xi, \mu_\zeta$ | separations in $\xi$ and $\zeta$ directions |
| $\rho$ | density of plate material (kg/m$^3$) |
| $\Phi_p$ | wall pressure spectral density (Pa$^2$/Hz) |
| $\omega$ | circular frequency (rad/s) |
| $\hat{\omega}_j$ | complex natural frequency of $j$th mode (rad/s) |

*Indices*

| | |
|---|---|
| $m, n, p, q, j$ | integer |

## References


[1] A.R. George, J.R. Callister, Aerodynamic noise of ground vehicles, SAE General Aviation Meeting, Wichita, KS, Paper No. 911027, 1991, pp. 1–28.

[2] K.-H. Kang, K.-J. Kim, Modal properties of beams and plates on resilient supports with rotational and translational complex stiffness, Journal of Sound and Vibration 190 (1996) 207–220.

[3] J. Park, L.G. Mongeau, Effects of seal mechanical properties on sound radiation from road vehicle side-glass windows, Proceedings of Inter-noise 99, Fort Lauderdale, FL, 1999, pp. 795–800.

[4] W.A. Strawderman, R.S. Brand, Turbulent-flow-excited vibration of a simply supported, rectangular flat plate, Journal of the Acoustical Society of America 45 (1968) 177–192.

[5] W.K. Blake, Mechanics of Flow-Induced Sound and Vibration, Vol. I and II, Academic Press Inc, New York, 1996.

[6] W.R. Graham, A comparison of models for the wavenumber-frequency spectrum of turbulent boundary layer pressures, Journal of Sound and Vibration 206 (1997) 541–565.

[7] F. Han, R.J. Bernard, L.G. Mongeau, Prediction of flow-induced structural vibration and sound radiation using energy flow analysis, Journal of Sound and Vibration 227 (1999) 685–709.

[8] A.W. Leissa, The free vibration of rectangular plates, Journal of Sound and Vibration 31 (1973) 257–293.

[9] M. Allen, N. Vlahopoulos, Noise generated from a flexible and elastically supported structure subject to turbulent boundary layer flow excitation, Finite Elements in Analysis and Design 37 (2001) 687–712.

[10] D. Young, Vibration of rectangular plates by the Ritz method, Journal of Applied Mechanics 17 (1950) 448–453.

[11] A. Berry, J.-L. Guyader, J. Nicolas, A general formulation for the sound radiation from rectangular, baffled plates with arbitrary boundary conditions, Journal of the Acoustical Society of America 88 (1990) 2792–2802.

[12] O. Beslin, J. Nicolas, A hierarchical functions set for predicting very high order plate bending modes with any boundary conditions, Journal of Sound and Vibration 202 (1997) 633–655.

[13] L. Meirovitch, Computational Methods in Structural Dynamics, Sijthoff & Noordhoff, Rockville MD, 1980.

[14] F. Fahy, Sound and Structural Vibration: Radiation, Transmission and Response, Academic Press, London, 1985.

[15] G. Chen, J. Zhou, Vibration and Damping in Distributed Systems Volume II: WKB and Wave Methods, Visualization and Experimentation, CRC Press, Boca Raton, FL, 1993.

[16] D.E. Newland, An Introduction to Random Vibrations, Spectral & Wavelet Analysis, Addison-Wesley Longman, Essex UK, 1993.

[17] G. Maidanik, Use of delta function for the correlations of pressure fields, Journal of the Acoustical Society of America 33 (1961) 1598–1606.
[18] F.R. Fricke, D.C. Stevenson, Pressure fluctuations in a separated flow region, Journal of the Acoustical Society of America 44 (1968) 1189–1200.
[19] J. Park, T. Siegmund, L. Mongeau, Influence of support properties on the forced vibrations of rectangular plates, Journal of Sound and Vibration, in press.